The International Journal of Advanced Manufacturing Technology (2020) 109:579–588
https://doi.org/10.1007/s00170-020-05509-1

ORIGINAL ARTICLE

Microstructure and mechanical characterization of TI6AL4V-B_4C metal ceramic alloy, produced by laser powder-bed fusion additive manufacturing

Alexander Golyshev[1] · Anatoly Orishich[1]

Received: 15 January 2020 / Accepted: 19 May 2020 / Published online: 6 July 2020
© Springer-Verlag London Ltd., part of Springer Nature 2020

Abstract
Increasing performance requirements of advanced products demands new, versatile fabrication techniques. Additive technology represents one of the most prospective fields of future production. B4C-based composites were fabricated on titanium substrate by selective laser melting (SLM) using titanium (Ti-6Al-4V) and boron carbide (B_4C) powder mixture at different weight ratio (Ti:B_4C = 1:0, 9:1, 8:2, and 7:3). It was shown that the use of a powder mixture B_4C + Ti-6Al-4V with ceramic concentration of more than 10% of weight led to formation of cracks. The microstructure of composites was studied by optical and electron microscopy. It was shown that a heterogeneous structure was formed with regular allocation of zones inside each layer. It was established that new chemical compounds (TiB, TiB_2, TiC) absent in the initial powder mixture were formed in the new structure. A significant change in microhardness is shown (for sample without ceramics—372 HV0.3, for sample 10% B_4C + 90% Ti-6Al-4V—from 548 to 4214 HV0.3). It was shown that the wear loss of B_4C-free sample is approximately 4.2 times higher than that of the sample with 10 wt% B_4C.

Keywords Selective laser melting (SLM) · Metal matrix composites (MMC) · Ti-6Al-4V · Boron carbide ceramics B_4C

1 Introduction

New materials development and manufacturing new parts on their base, which have unique performance characteristics and can operate at high thermal and mechanical loads, is one of the most relevant problems in the modern development of rocket building, engineering, and metallurgy. Additive technology (AM) for the manufacture of prototypes and functional products rises to an industrial level today and represents one of the most prospective fields of flexible future production. Today there are more than ten known methods and technologies in additive manufacturing of parts, and new ones appear every year. The most widely used AT for manufacturing of 3D parts is the selective laser melting (SLM) [1–3].

✉ Alexander Golyshev
alexgol@itam.nsc.ru

Anatoly Orishich
laser@itam.nsc.ru

[1] Khristianovich Institute of Theoretical and Applied Mechanics, Institutskaya Str. 4/1, Novosibirsk 630090, Russia

To improve the characteristics of the formed products, the metal-matrix composite (MMC) coatings whose mechanical properties are obtained from the relevant combination of reinforcing elements of the metal matrix, are used. For industrial application, several MMC kinds have been developed, including Al, Ti, Fe, Cu, Mg, and Ni based, reinforced either by fibers or particles.

Titanium is characterized by a high strength to weight ratio among metals, along with a high corrosion resistance. Creation of titanium composites opens the prospect for improved specific rigidity and high-temperature strength, reduced abrasive wear [4, 5]. TiB compound is recognized as one of the most advantageous reinforcing materials for titanium [6–9]. Metal composites have been highly sought due to their high compatibility, increased melting point, extreme hardness, excellent wearing quality, and corrosion resistance, in combination with perfect viscosity for deconstruction. Various research groups have developed the TiC–TiB_2 composite material or coating based on different template materials with the help of ex-situ (directly using the TiC and TiB_2 powder) [10–13] or in situ (using Ti and B_4C or other predecessor) [14–20]. Thus, the work [11] regarding TiC–TiB_2–Ni on the steel template studies the

microstructure and demonstrates the presence of good mechanical properties. It is established that the coating obtained with 20% added wt. TiB_2 has higher microhardness than the coating obtained with 10%.

Work [14] demonstrates that in situ produced TiC–TiB_2 composite provides for even distribution of reinforced particles, along with excellent interfacial bonding between particles that increases stability and viscosity of composite deconstruction as compared to ex situ produced composite. Consequently, the TiC–TiB_2 in situ development, i.e., the use of the initial Ti and B_4C powders, is a better prospect for the creation of metal ceramic composite.

Many works are devoted to the development of surface strengthening techniques by creating the metal ceramic coating with in situ produced TiC–TiB_2 mixture [15–19, 21–25]. Both laser radiation [15–19, 21] and electrical discharge arc (TIG cladded) [22, 24, 26, 27] were used as energy sources. Microstructure, phase composition, and mechanical properties of the metal deposit were studied. The coating has shown to have a hardness 3–4 times higher than the steel template [15].

However, very few studies have shown the impact of the changed ratio of initial mixture of Ti and B_4C powders on the microstructure and friction properties of multilayer composite coating [4].

This work studies the multilayer composite samples produced by selective laser melting (SLM) with the use of the prepacked Ti-6Al-4V and B_4C powder mixture with various weight ratios (Ti-6Al-4V + B_4C = 9:1, 8:2, and 7:3 wt.) and in situ synthesis TiB–TiC–TiB_2 mixture [28]. The main objective was to create the composite 3D material with minimum flaws and study the impact of the initial powder composition on microstructure and nanostructure, microhardness, and abrasive wear.

2 Materials and procedure of experiments

Prior to SLM, the Ti-6Al-4V and B_4C powder particles with different weight percentages were mixed with a Venus FTLMV-02 V-shaped mixer (Filtra Vibracion, Spain) for 1 h to obtain homogenous powder mixture. Samples of titanium alloy with dimensions of 50 mm × 50 mm × 5 mm were used as the substrate. The working mixture included the prismatic boron carbide powder B_4C (Fig.1a), with a mean size of $d = 40$ μm and spherically shaped Ti-6Al-4V powder (Fig.1b) with the size from 10 to 45 μm. The chemical composition of powders is given in Fig.1.

Prior to laser treatment, the mixed powders were pre-placed onto the surface of the substrate at a thickness of approximately 0.4 mm without any binding material (no pre-consolidation). The oxide layer from the as-received substrate surface was removed by polishing it against SiC abrasive paper and subsequent cleaning with acetone. Laser treatment of powder mixture was performed on a Sibir-4 complex developed at ITAM SB RAS, which includes a continuous-wave CO2 laser with a power up to 5 kW, beam parameter product (BPP) 4.7 mm × mrad, and the wavelength of the laser was 10.6 μm [29]. Laser beam has a circular polarization. A ZnSe lens with a focal distance of 254 mm focused the laser beam inward the material, onto the material surface, and above the material surface. Laser processing was conducted in helium shielding gas introduced through the two nozzles under the specimens at a pressure of 0.2 MPa. The laser processing parameters were selected as laser power 1000 W, scan speed 16.6 mm/min, beam diameter of 2 mm, and over lapped tracks of 50%. Prior to laser treatment substrate plate has room temperature.

Composites were ground with SiC abrasive paper and finally polished with diamond suspension to obtain a specular

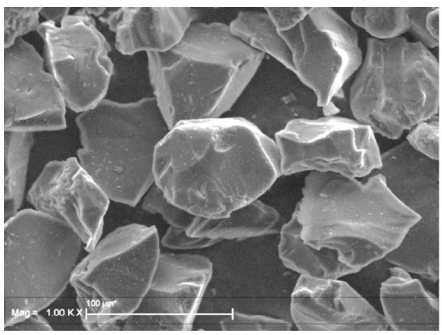

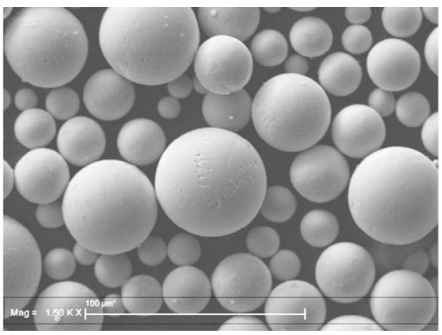

Fig. 1 SEM image from electronic microscope for B_4C (**a**) and Ti-6Al-4V (**b**) powder

Mass fraction, %						
B_4C	B	C	B_2O_3	Si	Fe	N
95,0	76,0	19,5	0,3	0,15	0,25	1,0

a

Mass fraction, %					
Ti	Al	V	Fe, O	N, C	Other
based	6,12	4,05	0,1	0,02	0,3

b

surface condition, using automatic polisher from Mecatech 334 to ensure good reproducibility. Thereafter, the specimens were placed in an ultrasonic bath and cleaned with demineralized water and dried with compressed air. Chemical etching of the samples was not carried out.

The formed tracks were studied on the optical confocal microscope Olympus LEXT OLS 3000. The microstructure was studied using a scanning electron microscope Zeiss EVO MA 15 equipped with two different detectors: a back-scattering electron detector to determine the phase composition and a secondary electron detector to analyze the surface microrelief. In addition, to assess the coating composition, an energy-dispersive X-ray spectrometer Oxford Instruments X-Max 80 mm^2 was used.

The microhardness was measured using a microhardness tester Wilson Hardness Group Tukon1102 by Vickers tester at a load of 300 g. Wear behavior of the composites that was evaluated using a testing is carried out by loading a sample pin against abrasive-coated paper supported on a solid backing (Fig. 2). The use of a spiral track on the abrasive paper achieves a steady process of wear by ensuring abrasion against fresh particles. The samples were created in the shape of a cylinder with a length of 10 mm and a diameter of 2 mm. Working surface's size is 2 × 2 mm, and its roughness before the test should not be higher than Ra = 2,5. The tests were carried out under applied loads of 10 N, rotated at 60 rpm, and 60-min application time in air. The weight loss of the specimens during the test was measured with an accuracy of ±0.0001 g. An average of three measurements was performed on each composites.

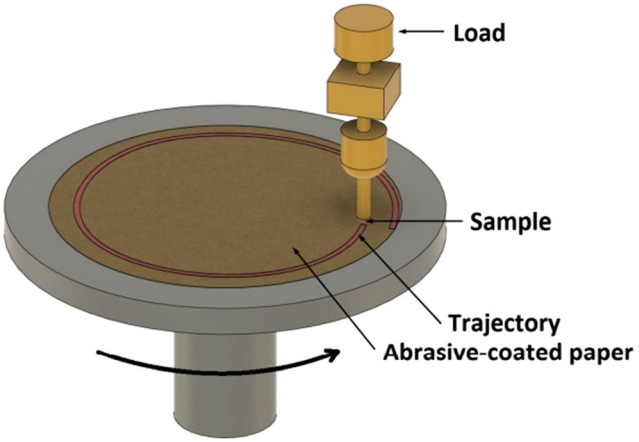

Fig. 2 Schematic illustration of the wear test

3 Experiment results

3.1 Optimization of laser effect mode during single track creation

This work provides for the optimization of track formation for four Ti-6Al-4V + B_4C powder mixture compositions (wt.): 1:0, 9:1, 8:2, and 7:3. Figure 3 illustrates typical photos from the optical microscope for track cross-sections with different powder mixture compositions of initial thickness of $t = 400$ μm. It should be noted that the dark areas inside the track represent initial boron carbide particles. No pores and cracks were detected inside the single tracks.

The single tracks after selective laser melting in cross-section represent a lens-shaped protrusion, with one part inside the template and the other over the template. Track cross dimensions are about 2 mm wide and 350–500 μm high. It should be noted that the ceramic concentration affects the shape and B_4C particle distribution in the track. With low concentration, the track upper surface is convex, and with B_4C (10% wt.) concentration, the ceramic particles are randomly distributed along the track section. With the B_4C concentration of 20% wt., the track upper surface is flat, and with B_4C concentration of 30% wt., it is concave. In both cases, the B4C ceramic particles are localized near the substrate boundary.

The built-up track surface roughness was analyzed by optical microscopy using the confocal microscope Olympus LEXT3000. Tables 1 and 2 represent roughness measurements R_z and R_a for single tracks with different ceramic content in the powder mixture based on scanning velocity V and focal spot position f.

In the course of laser exposure optimization, it was established that for all powder mixtures the high-quality single tracks (flaw-free and minimum roughness) are formed at $W = 1000$ W, $V = 0.7$ m/min., $f = -15$ mm. Using this mode, the arrays consisting of 4 tracks in horizontal plane and 8 layers by height are formed.

3.2 Track array microstructure

Figure 4 illustrates the microstructure of 3D array cross-section obtained from the optical microscope. It is obvious that with the ceramic concentration of 10% wt. the built-up array is homogeneous and crack-free; however, with the increased concentration by 20% wt. the lateral and transverse cracks are formed. For 30% wt., the produced sample has been completely destroyed.

Figure 4 shows that the B_4C ceramic particle distribution makes it possible to define all 8 layers that form the array. The detailed microstructure and nanostructure of typical individual layer of the array were studied using the electronic microscope (see Fig. 5). It is obvious from Fig. 5 that 3 equal zones can be defined inside each layer. Zone 1 represents a metal bond with boron carbide particles. The analysis of the composition of elements (see Fig. 6) shows that the metal matrix

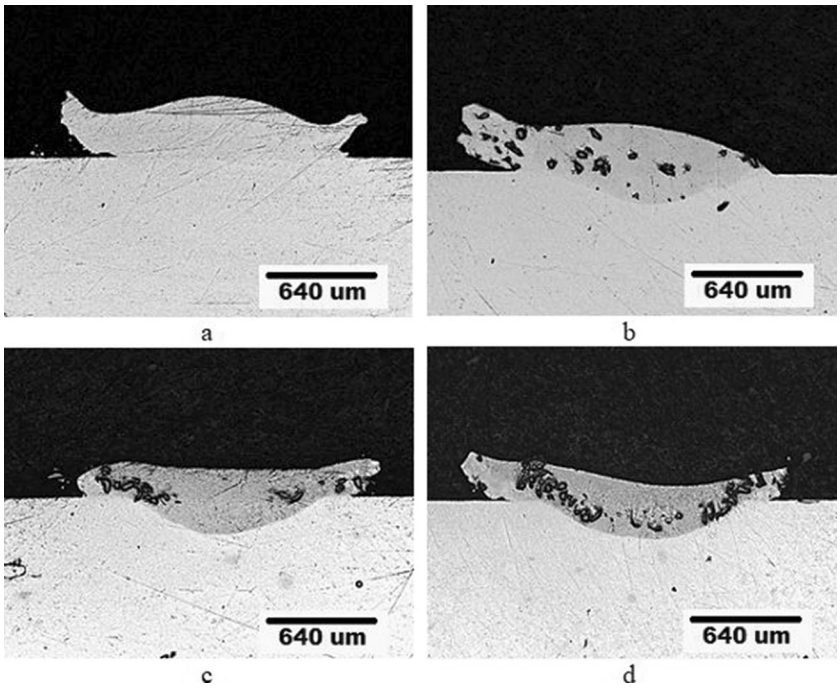

Fig. 3 Photos from the optical microscope for single tracks (**a** - Ti-6Al-4, **b** - B_4C – Ti-6Al-4V (1:9 wt.), **c** - B_4C – Ti-6Al-4V (2:8 wt.), **d** - B_4C – Ti-6Al-4V (3:7 wt.))

represents the initial powder mixture Ti-6Al-4V, and particles—B_4C. It should be noted that the initially prismatic boron carbide particles have changed their form after laser exposure and become well-rounded.

In zone 2 there are many different structures; it has a complex morphology; 3 different types of crystalline structures can be distinguished. Figures 5 and 7 illustrate this zone in details, separate areas are defined, and the composition of elements is determined. The darkest needle-shaped structures [19, 24] or whiskers [25] (spectrum 1; Fig. 7) represent the boron and titanium compound (TiB and TiB_2). The second structures represent the grains (approximate size of 1 μm) located along the entire perimeter of whiskers. It was established after elemental analysis (spectrum 2; Fig. 7) that these grains were titanium carbide TiC. The third structure of zone 2 represents a matrix arranged between whiskers. The elemental analysis has established that this area represents a metal matrix consisting of Ti-6Al-4V (spectrum 3; Fig. 7) with dissolved carbon. It should be noted that the potential increased carbon content in the titanium matrix was indicated in the work [24].

Figure 8 illustrates zone mapping by whiskers (zone 2). It can be seen that boron is concentrated in the long dark formations, while the carbon is on the boundaries of these formations. The metal alloy components are arranged only in the liquid-alloy, and titanium uniformly fills the entire image.

The third zone (Fig. 5) represents a transition zone arranged between zone 1 and zone 2. It can be seen that zone 3 represents a set of fine grains with a characteristic size of 2–3 μm. It was established during the elemental analysis that the picture was very similar to that of zone 2. In Fig. 5, the dark grain represents the boron and titanium compound (TiB and TiB_2), the light grain–boron carbide (TiC), and the gray area (3)–metal matrix Ti-6Al-4V.

Table 1 Surface roughness of single tracks depending on the parameter f ($V = 0.7$ m/min, $W = 1000$ W)

f, mm	Ti-6Al-4V		B_4C + Ti-6Al-4V 1:9 wt%		B_4C + Ti-6Al-4V 2:8 wt%	
	R_z, μm	R_a, μm	R_z, μm	R_a, μm	R_z, μm	R_a, μm
− 10	32.4	28	22.8	15.6	32	8.9
− 15	30.1	15.8	35.6	12.7	24	6.2
− 20	83.2	38	28.7	9.8	39.5	35.3

Table 2 Surface roughness of single tracks depending on the parameter V ($W = 1000$ W, $f = -15$ mm)

V, m/min	Ti-6Al-4V		B_4C + Ti-6Al-4V 1:9 wt%		B_4C + Ti-6Al-4V 2:8 wt%	
	R_z, μm	R_a, μm	R_z, μm	R_a, μm	R_z, μm	R_a, μm
0.7	33.4	12.2	41.5	10.8	19.5	14.5
1.1	30.1	15.8	35.6	12.7	24	6.2
1.5	36	15.9	36.7	8.5	40.5	14.2

3.3 Change of mechanical characteristics: Microhardness and wear quality of the produced coatings

The microhardness was measured in different cross-section areas of the built-up samples. The obtained data were averaged by 5 measurements in a row. Control measurements of the sample built-up by powder composition of 100% Ti-6Al-4V were conducted. It was established that the microhardness of the ceramic-free substrate (Ti-6Al-4V) was even over the entire volume varying within 372–404 HV0.3. When comparing with the reference data, it can be seen that the values are close (microhardness Ti-6Al-4V = 312 … 382).

Figure 5 illustrates the EDX image of the sample 10% B_4C + 90% Ti-6Al-4V. In this case, the heterogeneous structure with the zones having different mechanical characteristics is formed. The microhardness changing in different areas of the sample reaches a 3-fold value (from 548 to 1413 HV0.3). The microhardness measurement of the B_4C particle showed the value of 4214 HV0.3.

Figure 9 illustrates the photos of indented impressions in different zones within one built-up layer (see Fig. 5). It can be seen that in zone 2 and in zone 3 (see Fig. 5) the microhardness value is close and shows 1292 and 1253 HV0.3, respectively. Figure 9 c illustrates the photo showing the substrate-built-up layer boundary (zone 1; Fig. 5). The measurements have demonstrated that the microhardness of the solid solution of the built-up coating in 566 HV0.3 is higher in this area than the microhardness of the substrate 367 HV0.3.

Wear resistance testing was conducted for two samples Ti-6Al-4V and 10% B4C + 90% Ti-6Al-4V. The data were averaged from three measurements. Table 3 provides wear loss. The wear loss of B4C-free sample is approximately 4.2 times than that of the sample with 10 wt% B4C.

4 Discussion of results

The composite metal ceramic 3D samples are produced by the use of various mixtures of B_4C ceramic powders and Ti-6Al-4V alloy using a layer-by-layer application of the powder mixture and selective laser sintering.

The macromorphology of individual track cross-sections and multilayer samples is considerably different. The applied layer and template interface are very clear and continuous; no lamination is observed indicating excellent metal bond with the template. The coating surface is relatively smooth, R_z = 20–30 μm and R_a = 6–15 μm.

In the mechanism of track shape formation and ceramic particle distribution by volume, the convective mass transfer is likely to play a key role as compared to the diffusive one. The main reason and driving forces of convection are the

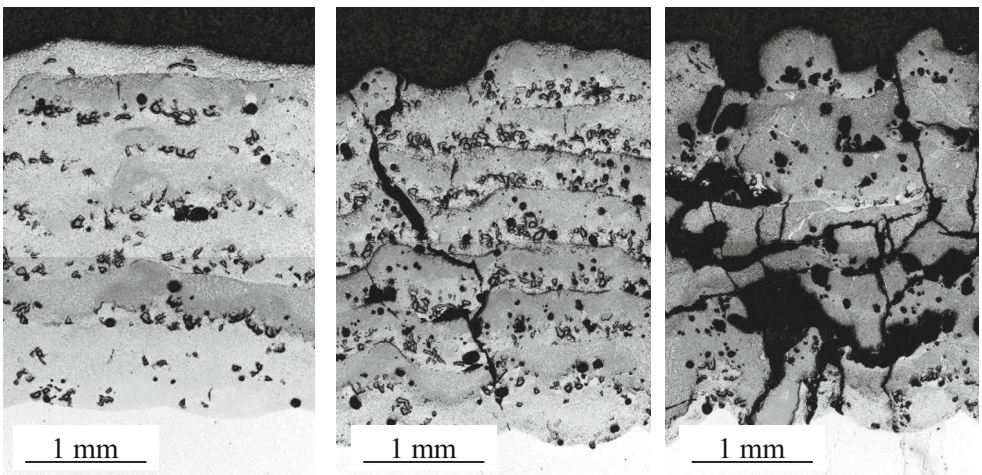

Fig. 4 Optical photos of 3D array cross-sections B_4C + Ti-6Al-4V (**a** - B_4C – Ti-6Al-4V (1:9 wt.), **b** - B_4C – Ti-6Al-4V (2:8 wt.), **c** - B_4C – Ti-6Al-4V (3:7 wt.))

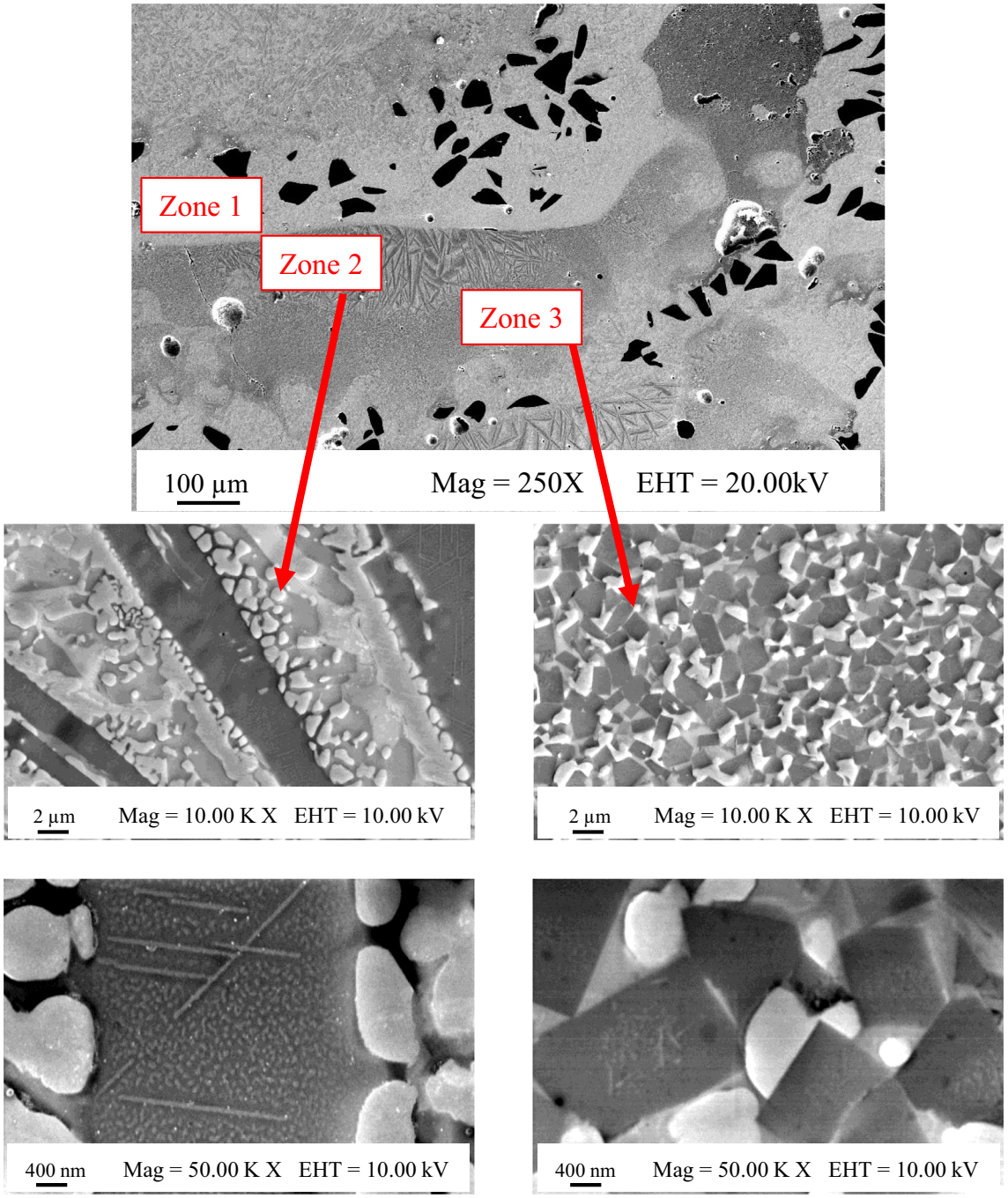

Fig. 5 SEM image of nanostructure and microstructure of individual layer of the array with the mixture composition of B_4C + Ti-6Al-4V 1:9 wt%

surface-tension gradients. During laser-induced heating, the temperature of the material is at maximum in the center of the beam and decreases in the direction of the edges. The surface tension of the liquid (liquid alloy) depends on the temperature and usually reduces with the temperature increase. As a consequence, the force directed from the center to the edges of the light spot occurs on the surface, and the liquid starts flowing and that finally leads to the formation of cylindrical concave meniscus. This was the situation observed at high ceramic concentration in the powder mixture (see Fig. 3; 30% B_4C + 70% Ti-6Al-4V). In its turn, at lower B_4C concentration (Fig. 3; 10% B_4C + 90% Ti-6Al-4V) without it (100% Ti-6Al-4 V) the tension and temperature dependence changed the conditions that provided for formation of convex cylindrical meniscus. At the concentration of 20% B_4C + 80% Ti-6Al-4V, the meniscus surface was flat. It is worth noting that for all studied concentrations the tracks had no cracks and pores.

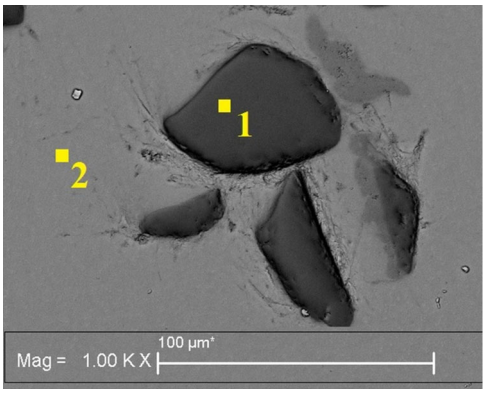

Fig. 6 SEM/EDX point analysis at the zone 1 of composite B_4C + Ti-6Al-4V 1:9 wt%

Element	1 Atomic %	2 Atomic %
B	74.62	0
C	25.18	2.46
Al	0	6.60
Ti	0.17	87.13
V	0	3.81
Other	Si (0.03)	0

The situation drastically changed with the creation of multilayer coating. In this case, at the initial mixture concentration of 20% B_4C + 80% Ti-6Al-4V there already appeared cracks (see Fig. 4), and at concentration of 30% B_4C + 70% Ti-6Al-4V the sample completely collapsed. Such differences appeared to be due to the titanium ingress from the template to the first layer track liquid alloy that produced changes in the metal and ceramic concentration ratio. This shows that during creation of 3D parts the maximum share of the ceramic weight must be less than 20%. It should be noted that this condition of implementation of a laser multilayer crack-free alloyage that corresponds to the requirement consisting of the number of boron atoms in the volume unit of the initial powder should be less than that of the titanium atoms.

The chemical reactions occurring in the layer are critical because they are useful for predicting the nature and property of the created material. It is known that at high temperatures the boron carbide provokes chemical reaction with titanium resulting in new chemical compounds (TiB, TiB_2, TiC) [16, 22, 24, 26]:

$$5Ti + B_4C \rightarrow 4TiB + TiC \quad (1)$$

$$3Ti + B_4C \rightarrow 2TiB_2 + TiC \quad (2)$$

$$B_4C \rightarrow 4B + C \quad (3)$$

$$Ti + TiB_2 \rightarrow 2TiB \quad (4)$$

The work [16] provides for the calculation of change in standard Gibbs free energy of reactions (1)–(2) with the use

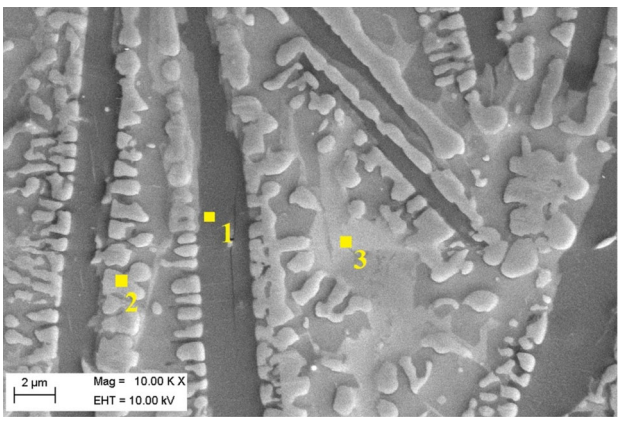

Fig. 7 SEM/EDX point analysis at the zone 2 of composite B_4C + Ti-6Al-4V 1:9 wt%

Element/Spectrum	1 Weight %	1 Atomic %	2 Weight %	2 Atomic %	3 Weight %	3 Atomic %
B	40.49	65.65	-	-	-	-
C	11.49	16.77	20.58	50.83	15.89	40.83
Ti	48.02	17.57	79.42	49.17	67.24	43.32
Al	-	-	-	-	10.48	11.98
V	-	-	-	-	6.39	3.87

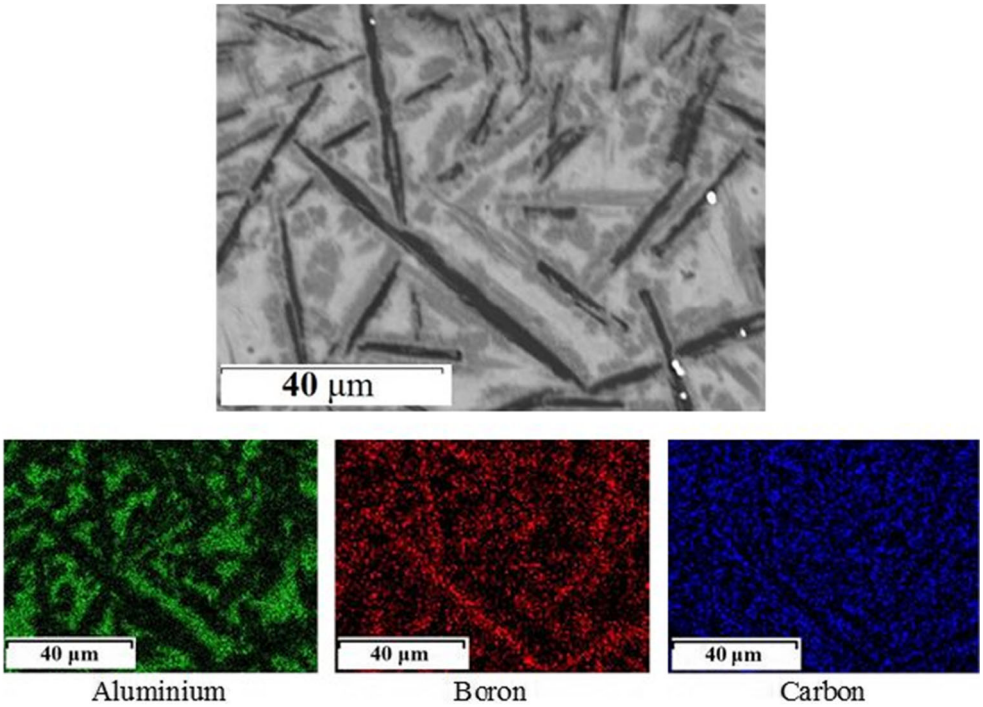

Fig. 8 Zone 2 mapping by whiskers for powder mixture sample B_4C + Ti-6Al-4V 1:9 wt%

of thermodynamic data. Fully complying with previous studies [see, for example, [15–19, 21]] during laser melting of the B_4C + Ti-6Al-4V powder mixture, after solidification of the liquid alloy, the microstructural analysis on the basis of the SEM image clearly explains the morphology of the formed phases, i.e., the presence of various structures in the created built-up material. Large (20–50 μm) fused particles of non-reacted ceramics B_4C are observed (see Fig. 6). The dark structures associated with TiB phases are represented in the form of whiskers with characteristic sizes: 2–3 μm diameter and 30–50 μm long. It should be noted that such large TiB needles are detailed in [19] demonstrating their complex structure and hollow core filled with titanium cores, in particular. Previous multiple studies [see, for example, [24, 30, 31]], as well as our EDS analyses (Fig. 7) showed that the dark hexagonal prismatic or rectangular particles of about 1 μm were formed by the TiB_2 phase and light structures (see Fig. 5), and the round-shaped ones represented the TiC phase. In addition to the clear structures of the TiC, TiB phases, there is also some amount of the metal bond of titanium alloy Ti-6Al-4V (see Fig. 7).

It is worth noting that a brand new property of the structure of the built-up material was observed in our experiments during creation of multilayer samples. The alloy separation during solidification was found for the first time, i.e., the formation of three zones with clear boundaries inside each layer applied (see Fig. 5). Previously, during study of the single-layer coatings of surface strengthening with the use of the B_4C + Ti or TiB, or TiC powder mixtures, the formation of such zones was not observed [1, 2, 4–7, 10–12]. The important feature of these zones is the difference in the morphology; each zone has its own set of phases. There are TiB and TiC in the upper zone (3), while TiB_2 and TiC in the medium zone (3). At this, if in the medium zone the hexagonal prismatic or rectangular particles TiB_2 and round ones TiC are arranged in a random way, in the upper zone the structures of the round particle TiC location along the TiB phase surface represented as whiskers (see Fig. 5) are observed. It can be supposed that

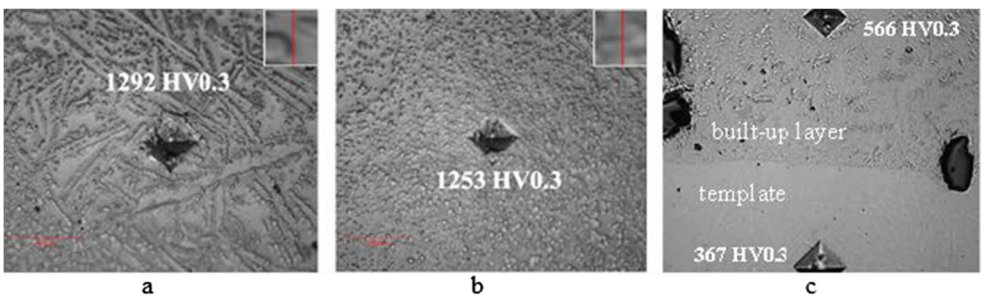

Fig. 9 Images of the sample B_4C + Ti-6Al-4V 1:9 wt% with indenter impressions in different areas: **a** zone 2, **b** zone 3, and **c** zone 1 in Fig. 5

Table 3 Wear resistance of the obtained composites

	Ti-6Al-4V	B_4C + Ti-6Al-4V 1:9 wt%
Initial weight (g)	0.1441	0.1382
Final weight (g)	0.1322	0.1354
Initial and final weight difference (g)	0.0119	0.0028

the formation of such a structure is due to the temperature gradient and by the track depth with the layer applied at the stage of the liquid alloy solidification and, as a consequence, the difference of the formed crystalline ceramic phases. During the laser radiation exposure, powerful convective movements related to the surface tension gradient providing for complete stirring of the liquid alloy are implemented. Further cooling of the liquid alloy is determined by the energy flow to the lower layers of the built-up sample. That is why the solidification starts from the lower layer surface without nucleation. Thus, the lower zone of the liquid alloy (zone 1, Fig. 5) had the minimum temperature, and this is the area where the remaining nondissolved particles of the initial B_4C ceramics are recorded. The upper zone (zone 2; Fig. 5) having the maximum temperature is characterized by formation of whiskers in the form of fine needles. The recent work [24] when studying the effect of the energy contribution on the microstructure showed that the TiB crystalline formation in the form of the needle whiskers was observed at high arc currents, 60 A, and more, i.e., at higher temperatures. Simultaneously, the application of small currents 50 A (Fig. 8a in work [24]), i.e., lower temperatures of the liquid alloy, provides for the formation of the cubic and hexagonal TiB_2 crystallines. In our case, such crystalline structures are formed in medium zone 3 at the intermediate temperature.

The detailed discussion of the coating microstructure along its depth was provided in work [26], for example. It is noted that after complete melting and respective mixing of the coating material and liquid material of the subsurface template during solidification, various coating morphology types appear from the melted bath depending on the rate of solidification. At first, TiC solidifies (melting point of 3160 °C) and appears in the round-shaped particles or dendritic structure. With further cooling-down, the liquid alloy TiB_2 (melting point of 2970 °C) starts nucleating and solidifies in the form of hexagonal or rhombohedral structures that fully corresponded to the formation of intermediate zone 3, in our case.

5 Conclusion

Using continuous laser radiation, optimization of the laser effect on powder mixture Ti-6Al-4V + B_4C with mass concentration ratios of 1:0, 9:1, 8:2, and 7:3 was conducted. It was shown that the use of powder mixture Ti-6Al-4V + B_4C with ceramic concentration of more than 20% is not desired as it leads to formation of cracks. The optimization resulted in the formation of metal ceramic crack-free 3D structure with ceramic concentration of 10% wt.

1. The roughness values of the high-quality single tracks (flaw-free) were determined (R_z varies within 25… 35 μm depending on the ceramic concentration). Significant change in microhardness is shown (for sample without ceramics—372 HV0.3, for sample 10% B_4C + 90% Ti-6Al-4V—from 548… to 4214 HV0.3).
2. It was shown that the wear loss of B_4C-free sample is approximately 4.2 times than that of the sample with 10 wt% B4C.
3. The coating microstructure was studied by optical and electron microscopy. It was established that new chemical compounds (TiB, TiB_2, TiC) absent in the initial powder mixture were formed in the built-up structure.
4. It was shown that the heterogeneous structure had a regular allocation of zones formed inside each cladding layer. And each zone is characterized by its set of phases, structures of ceramic crystalline structures, and respective microhardness value.

Funding information The work is the supported by the grant of the Russian Scientific Foundation No. 18-79-00052.

References

1. DebRoy T, Wei HL, Zuback JS et al. (2018) Additive manufacturing of metallic components - Process, structure and properties. Prog Mater Sci 92:112–224. https://doi.org/10.1016/j.pmatsci.2017.10.001
2. MIRACLE D (2005) Metal matrix composites—from science to technological significance. Compos Sci Technol 65:2526–2540. https://doi.org/10.1016/j.compscitech.2005.05.027
3. Xiao Z, Chen Y, Georgiadis A, Liu J, Zhou X, Zhang Z (2018) Analysis of brittle layer forming mechanism in Ti6Al4V sloping structures by SLM technology. Int J Adv Manuf Technol 98:1783–1789. https://doi.org/10.1007/s00170-018-2296-z
4. Pouzet S, Peyre P, Gorny C, Castelnau O, Baudin T, Brisset F, Colin C, Gadaud P (2016) Additive layer manufacturing of titanium matrix composites using the direct metal deposition laser process. Mater Sci Eng A 677:171–181. https://doi.org/10.1016/J.MSEA.2016.09.002
5. Cai C, Song B, Qiu C, Li L, Xue P, Wei Q, Zhou J, Nan H, Chen H, Shi Y (2017) Hot isostatic pressing of in-situ TiB/Ti-6Al-4V composites with novel reinforcement architecture, enhanced hardness and elevated tribological properties. J Alloys Compd 710:364–374. https://doi.org/10.1016/j.jallcom.2017.03.160
6. Ravi Chandran KS, Panda KB, Sahay SS (2004) TiBw-reinforced Ti composites: processing, properties, application prospects, and research needs. JOM 56:42–48. https://doi.org/10.1007/s11837-004-0127-1

7. Fomin VM, Golyshev AA, Kosarev VF, Malikov AG, Orishich AM, Ryashin NS, Filippov AA, Shikalov VS (2017) Creation of heterogeneous materials on the basis of B4C and Ni powders by the method of cold spraying with subsequent layer-by-layer laser treatment. J Appl Mech Tech Phys 58:947–955. https://doi.org/10.1134/S0021894417050224
8. Hu Y, Ning F, Wang H, Cong W, Zhao B (2018) Laser engineered net shaping of quasi-continuous network microstructural TiB reinforced titanium matrix bulk composites: microstructure and wear performance. Opt Laser Technol 99:174–183. https://doi.org/10.1016/J.OPTLASTEC.2017.08.032
9. Neikter M, Huang A, Wu X (2019) Microstructural characterization of binary microstructure pattern in selective laser-melted Ti-6Al-4V. Int J Adv Manuf Technol 104:1381–1391. https://doi.org/10.1007/s00170-019-04002-8
10. Li W-J, Tu R, Goto T (2006) Preparation of directionally solidified TiB2–TiC eutectic composites by a floating zone method. Mater Lett 60:839–843. https://doi.org/10.1016/j.matlet.2005.10.028
11. Liu J, Liu Z (2010) An experimental study on synthesizing TiC–TiB2–Ni composite coating using electro-thermal explosion ultra-high speed spraying method. Mater Lett 64:684–687. https://doi.org/10.1016/J.MATLET.2009.12.038
12. Ravnikar D, Dahotre NB, Grum J (2013) Laser coating of aluminum alloy EN AW 6082-T651 with TiB2 and TiC: microstructure and mechanical properties. Appl Surf Sci 282:914–922. https://doi.org/10.1016/J.APSUSC.2013.06.089
13. Diao Y, Zhang K (2015) Microstructure and corrosion resistance of TC2 Ti alloy by laser cladding with Ti/TiC/TiB2 powders. Appl Surf Sci 352:163–168. https://doi.org/10.1016/J.APSUSC.2015.04.030
14. Ramesh CS, Ahamed A (2011) Friction and wear behaviour of cast Al 6063 based in situ metal matrix composites. Wear 271:1928–1939. https://doi.org/10.1016/J.WEAR.2010.12.048
15. Du B, Paital SR, Dahotre NB (2008) Phase constituents and microstructure of laser synthesized TiB2–TiC reinforced composite coating on steel. Scr Mater 59:1147–1150. https://doi.org/10.1016/J.SCRIPTAMAT.2008.07.035
16. Li J, Yu Z, Wang H, Li M (2010) Microstructural characterization of titanium matrix composite coatings reinforced by in situ synthesized TiB + TiC fabricated on Ti6Al4V by laser cladding. Rare Metals 29:465–472. https://doi.org/10.1007/s12598-010-0151-y
17. Bai LL, Li J, Chen JL, Song R, Shao JZ, Qu CC (2016) Effect of the content of B4C on microstructural evolution and wear behaviors of the laser-clad coatings fabricated on Ti6Al4V. Opt Laser Technol 76:33–45. https://doi.org/10.1016/J.OPTLASTEC.2015.07.010
18. Li J, Yu Z, Wang H, Li M (2010) Microstructural evolution of titanium matrix composite coatings reinforced by in situ synthesized TiB and TiC by laser cladding. Int J Miner Metall Mater 17:481–488. https://doi.org/10.1007/s12613-010-0345-1
19. Kooi B, Pei Y, De Hosson JT (2003) The evolution of microstructure in a laser clad TiB–Ti composite coating. Acta Mater 51:831–845. https://doi.org/10.1016/S1359-6454(02)00475-5
20. Wu Y, Wang AH, Zhang Z, Xia HB, Wang YN (2015) Microstructure, wear resistance and cell proliferation ability of in situ synthesized Ti–B coating produced by laser alloying. Opt Laser Technol 67:176–182. https://doi.org/10.1016/J.OPTLASTEC.2014.10.009
21. Tang J (2016) Mechanical and tribological properties of the TiC–TiB2 composite coating deposited on 40Cr-steel by electro spark deposition. Appl Surf Sci 365:202–208. https://doi.org/10.1016/J.APSUSC.2015.12.198
22. Tijo D, Masanta M (2017) Mechanical performance of in-situ TiC–TiB2 composite coating deposited on Ti-6Al-4V alloy by powder suspension electro-discharge coating process. Surf Coat Technol 328:192–203. https://doi.org/10.1016/J.SURFCOAT.2017.08.048
23. Tijo D, Masanta M, Das AK (2018) In-situ TiC-TiB2 coating on Ti-6Al-4V alloy by tungsten inert gas (TIG) cladding method: part-I. Microstructure evolution. Surf Coat Technol 344:541–552. https://doi.org/10.1016/J.SURFCOAT.2018.03.082
24. Tijo D, Masanta M (2019) Effect of Ti/B4C ratio on the microstructure and mechanical characteristics of TIG cladded TiC-TiB2 coating on Ti-6Al-4V alloy. J Mater Process Technol 266:184–197. https://doi.org/10.1016/J.JMATPROTEC.2018.11.005
25. An Q, Huang L, Jiang S, Li X, Gao Y, Liu Y, Geng L (2017) Microstructure evolution and mechanical properties of TIG cladded TiB reinforced composite coating on Ti-6Al-4V alloy. Vacuum 145:312–319. https://doi.org/10.1016/J.VACUUM.2017.09.019
26. Tijo D, Masanta M (2018) In-situ TiC-TiB2 coating on Ti-6Al-4V alloy by tungsten inert gas (TIG) cladding method: part-II. Mechanical performance. Surf Coat Technol 344:579–589. https://doi.org/10.1016/j.surfcoat.2018.03.083
27. WANG Z, ZHOU X, ZHAO G (2008) Microstructure and formation mechanism of in-situ TiC-TiB2/Fe composite coating. Trans Nonferrous Metal Soc China 18:831–835. https://doi.org/10.1016/S1003-6326(08)60144-2
28. Fereiduni E, Ghasemi A, Elbestawi M (2019) Selective laser melting of hybrid ex-situ/in-situ reinforced titanium matrix composites: Laser/powder interaction, reinforcement formation mechanism, and non-equilibrium microstructural evolutions. Mater Des 184:108185. https://doi.org/10.1016/j.matdes.2019.108185
29. Golyshev AA, Orishich AM, Filippov AA (2019) Similarity laws in laser cladding of cermet coatings. J Appl Mech Tech Phys 60:758–767. https://doi.org/10.1134/S0021894419040217
30. Akhtar F (2008) Microstructure evolution and wear properties of in situ synthesized TiB2 and TiC reinforced steel matrix composites. J Alloys Compd 459:491–497. https://doi.org/10.1016/j.jallcom.2007.05.018
31. Wang HY, Jiang QC, Zhao YQ, Zhao F, Ma BX, Wang Y (2004) Fabrication of TiB2 and TiB2–TiC particulates reinforced magnesium matrix composites. Mater Sci Eng A 372:109–114. https://doi.org/10.1016/J.MSEA.2003.10.250

Publisher's note Springer Nature remains neutral with regard to jurisdictional claims in published maps and institutional affiliations.